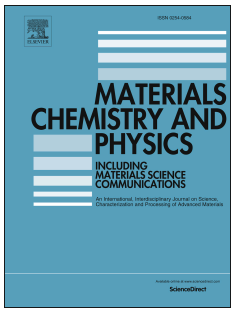

Synthesis and characterization of $NiFe_2O_4$ nanoparticles as reusable magnetic nanocatalyst for organic dyes catalytic reduction: Study of the counter anion effect

Cheikh Reda Bernaoui, Abdelaziz Bendraoua, Farouk Zaoui, Juan Jesús Gallardo, Javier Navas, Rafik Abdelkrim Boudia, Houria Djediai, Nor el Houda Goual, Mehdi Adjdir

PII: S0254-0584(22)01099-9

DOI: https://doi.org/10.1016/j.matchemphys.2022.126793

Reference: MAC 126793

To appear in: *Materials Chemistry and Physics*

Received Date: 5 May 2022

Revised Date: 16 August 2022

Accepted Date: 15 September 2022

Please cite this article as: C.R. Bernaoui, A. Bendraoua, F. Zaoui, Juan.Jesú. Gallardo, J. Navas, R.A. Boudia, H. Djediai, N.e.H. Goual, M. Adjdir, Synthesis and characterization of $NiFe_2O_4$ nanoparticles as reusable magnetic nanocatalyst for organic dyes catalytic reduction: Study of the counter anion effect, *Materials Chemistry and Physics* (2022), doi: https://doi.org/10.1016/j.matchemphys.2022.126793.

Author statement

Cheikh Reda Bernaoui: Conceptualization, Validation, Methodology, Visualization, Writing- original draft, Software, Investigation, Data Curation. **Abdelaziz Bendraoua:** Writing - review & editing, Project administration. **Farouk Zaoui:** Writing- original draft, Review & editing, Software, Conceptualization, Visualization, Validation, Investigation, Data Curation, Project administration, Resources. **Juan Jesús Gallardo:** Writing - Review & Editing. **Javier Navas:** Writing - review & editing, Resources. **Rafik Abdelkrim Boudia:** Formal analysis, Writing - review & editing. **Houria Djediai:** Writing - Review & Editing. **Nor el Houda Goual:** Writing - Review & Editing. **Mehdi Adjdir:** Formal analysis, Writing - review & editing, Conceptualization.

Graphical Abstract:

Synthesis and characterization of $NiFe_2O_4$ nanoparticles as reusable magnetic nanocatalyst for organic dyes catalytic reduction: Study of the counter anion effect.

Cheikh Reda Bernaoui[1*], Abdelaziz Bendraoua[1], Farouk Zaoui[2,3**], Juan Jesús Gallardo[4], Javier Navas[4], Rafik Abdelkrim Boudia[5], Houria Djediai[6], Nor el Houda Goual[1], Mehdi Adjdir[5]

[1] Laboratory Organic Synthesis, Physical-Chemical and Environment, Department Chemistry, University of Science and Technology – Mohamed BOUDIAF-, USTO-MB, 31000, Oran, Algeria.
[2] Laboratoire de Chimie Physique Macromoléculaire, Université Oran1 Ahmed Ben Bella, B.P 1524 El-Menaouer, 31000, Oran, Algeria.
[3] Centre Universitaire ElCherif Bouchoucha -Aflou-, B.P 306, Aflou, Laghouat, Algeria.
[4] Departamento de Química Física, Facultad de Ciencias, Universidad de Cádiz, E-11510 Puerto Real (Cádiz), Spain.
[5] Applied Organic Synthesis Laboratory, Department of Chemistry, Faculty of Science, University of Oran, BP 1524, El Menaouar Oran 31000, Algeria.
[6] Laboratory of science technology and process engineering LSTGP, Department Chemistry, University of Science and Technology – Mohamed BOUDIAF-, USTO-MB, 31000, Oran, Algeria.

Corresponding authors, E-mail address:

Farouk Zaoui: zafarouk@hotmail.fr

Cheikh Reda Bernaoui: cheikhreda.bernaoui@univ-usto.dz - bernaouiredac@gmail.com

Abstract

This work concerns the preparation of $NiFe_2O_4$ with different counter ions using co-precipitation method to control their crystallite size, the materials were used as catalysts for the photocatalytic reduction of Methylene blue and Orange G dyes. Different characterization methods such as XRD, XPS, FTIR, SEM/EDS, VSM, and Zeta potential were employed for more information on our materials. The obtained results show clearly that the nature of the counter ions influences significantly the phase purity and crystallite size of $NiFe_2O_4$ nanoparticles. To study the individual contribution of crystallite size and lattice strain Scherrer formula, Williamson-Hall, and size strain plot calculation methods were employed. The results showed also that the material containing the purest phase and finer size was the best catalyst for the reduction of both dyes; the "NFCP" catalyst allowed a complete conversion of MB and OG dyes in a reaction time of 8 min and 4 min respectively. A study of the reusability was carried out and the obtained results showed that the catalyst can be reused more and more without losing its efficiency even after 5 cycles thus, confirming its stability. The phase purity, crystallite size, the counter ions difference, and the synergy between metals and the surface charge were the key parameters affecting the catalytic property.

Keywords: Nickel Ferrite, Counter-ion, Magnetic property, Organic dyes, Catalytic reduction.

1. Introduction

One of the most problems that have been bothering the scientific community in recent years is environmental pollution. Organic pollutants and especially dyes from the textile, leather, and printing industries, which are discharged into surface waters and groundwater, cause serious damage to the human health as well as to other living species every year [1-3]. The very stable structure of these pollutants and their non-biodegradability makes these molecules difficult to be eliminated. For this reason, different methods such as adsorption [4], coagulation, biological

treatment [5] , membrane treatment, and advanced oxidation processes [6-11] are commonly used for wastewater treatment [12-14]. However, catalytic reduction remains one of the most widely used and beneficial methods as it has the advantages of being efficient, fast, environmentally friendly, and cheap in contrast to other methods which are generally expensive, slow, and complicated to apply [15, 16]. Thus, it is important to look for and develop a good catalyst that is easy to prepare, low cost, effective, easy to recover, and reusable. Among the wide range of existing catalysts, magnetic materials have received particular interest for their various advantages such as the large specific surface area, low cost, easy preparation, easy recovery, reuse, and high photoreduction activity [17]. Nickel ferrite $NiFe_2O_4$ has obtained a lot of attention due to its magnetic proprieties and wide application fields such as technological, biomedical, catalysis ,and environmental [18-20]. On the basis of magnetic fields and composition MFe_2O_4 ferrites where M is a divalent cation namely Ni, Co, Zn, Fe… are classified according to their normal, inverse and mixed structures depending on the synthesis method [21-23]. The general formula of spinel ferrites is AB_2O_4 where A and B are metal cation located at distinct crystallographic positions when A represent (Ni^{2+}) at octahedral sites and B represent (Fe^{3+}) at tetrahedral sites. [24, 25] However, the nature of the selected metal cation and their arrangement at sites of crystallographic structures A and B can affect the physical properties of ferrites [23, 26]. Anti-parallel spins between Ni^{2+} and Fe^{3+} ions create ferromagnetic properties of nickel ferrite which provide various qualities such as high magnetic sensitivity, low-temperature synthesis, high coercive force, and super-paramagnetic [27, 28]. Different methods have been suggested for the preparation of nickel ferrite as chemical co-precipitation [27, 29], hydrothermal method [30], self-combustion method [31], sol-gel method [32], sol–gel auto-combustion method [33], microwave-combustion method [34]. However, controlling the size of the obtained metal oxide remains the main problem that has been the research subject of several scientific groups. Indeed, it has been reported that the size of the

nanoparticles is a very influential parameter on their physicochemical properties and catalytic activities, more the size is small more the activity is superior [35, 36]. Several factors can influence the size of the obtained nickel ferrite nanoparticles, including synthesis method, pH, temperature used, pressure, and also the cation counter ion chosen [37, 38]. For more precision of crystallite size determination and impact strain contributions, many methods such as Scherrer equation, Williamson Hall plot (W-H), and SSP method are used [39, 40]. The main objective of this work is to vary the iron counter ion between chloride and sulphate ions during the preparation of nickel ferrite nanoparticles to obtain a $FeCl_2$ based nickel ferrite sample and a $FeSO_4$ based sample. A calculation of crystallite size of $NiFe_2O_4$ via Scherrer equation, Williamson Hall uniform deformation model (UDM), and the size-strain plot method (SSP) with the estimation of (ε) value were done for both catalysts. A comparative study of the structural and morphological properties, as well as its photoreduction activity via the cationic dye methylene blue reduction and anionic dye orange G, is then performed. As nickel ferrite is a magnetic product and therefore is reusable and easy to separate, the obtained catalysts were tested, washed, and then reused several times to evaluate their recycling efficiency.

2. Experiment method

2.1.Materials and method

The reagents used in this study are: Nickel (II) nitrate (98.5%, Sigma-Aldrich), Iron(II) chloride (97%, Sigma-Aldrich), Iron(II) sulphate (97%, Sigma-Aldrich), Sodium Borohydride (99%, Sigma-Aldrich), Methylene Blue (Sigma-Aldrich), Orange G (Sigma-Aldrich) and distilled water was used in all experiments as a solvent.

2.2 Materials characterization

The XRD diffraction patterns were performed on Brucker D8 diffractometer with a CuKα radiation source ($\lambda_{CuK\alpha}$ = 1.540598 Å) at 45 kV and 30 mA data was collected from 2θ = (20 to 100°) at a scan step size of 0.016711 using 200.255 time per step. The surface composition and

chemical state of material was measured by XPS analysis on a Thermo Scientific K-Alpha spectrometer utilizing a monochromatic AlKα X-ray source. The Functional groups of all samples were analysed by FTIR spectra in the range 4000-500 cm^{-1} using a Bruker Tensor 37. The morphology of the $NiFe_2O_4$ samples were observed by Scanning electron microscopy (SEM) images on LEO-1455VP with a JEM-200 CX Transmission electron microscope (JOEL Belgium), the energy-dispersive X-ray spectroscopy (EDX) was performed by the same previous morphological equipment's. Vibrating sample magnetometer (QD-VSM) exhibits magnetic measurements of samples applied magnetic field sweep between ±8,000 Oe at room temperature. The surface charge were analysed by Zeta potential on the Zeta PALS, Brookhaven Instrument Comp USA. The reduction reaction of organic dyes was studied by UV-vis spectrophotometry (JENWAY 6800UV/Vis). The pH values were adjusted by AD1030 pH/mV.

2.3. Preparation of $NiFe_2O_4$ nanoparticles

The materials were prepared by co-precipitation method according to the literature [25]. Firstly, an iron solution were prepared by dissolving 1.04 g of $FeSO_4.6H_2O$ in 10 mL of distilled water, the solution was added drop wisely to a $Ni(NO_3)_2.6H_2O$ solution (0.29 g/10 mL). The mixture was stirred before adding a solution of NaOH (0.5 M) in order to obtain a pH =10. The general solution was stirred mechanically 40 min at the temperature of 70°C, the obtained solid $NiFe_2O_4$ nanoparticles were recovered by an external magnet, washed several times and dried for 8 h at 90°C, the final product has been called NFSP. The second sample "NFCP" were synthesized by the same procedure but by using 1.36 g $FeCl_2.6H_2O$ instead of the $FeSO_4.6H_2O$.

3. Catalytic test

The obtained nanoparticles were used as catalysts for the reduction of organic dyes (Methylene blue and Orange G), the reduction experiments were carried out at room temperature with two

different counter ions of $NiFe_2O_4$ as catalysts and $NaBH_4$ as a reducing agent [41, 42]. Firstly, 2 mL of Methylene Blue (MB) or Orange G (OG) pollutants (0.6 mM) was mixed with 2 mg of catalyst in a quartz cuvette, then 1.5 mL of freshly prepared $NaBH_4$ solution (0.2 M) was added to the suspension and quickly transferred to a UV–vis spectrophotometer. The evolution of the catalytic reduction of both photocatalysts was followed by UV-vis spectrophotometry (JENWAY 6800UV/Vis) by making a scan every minute. After finishing the reduction process, the catalyst was attracted by a simple magnet and washed several times with distilled water before being reused for a new cycle. Adsorption tests were taken into consideration without adding $NaBH_4$ (time was set at 15 min) the results demonstrated that the adsorption capacity of both catalysts is practically negligible. The first-order kinetic model was applied to determine the rate constant Kapp (min^{-1}), this model is described by the Eq. (1).

$$LnC_t/C_0=lnA_t/A_0 = -Kapp \times t \quad (1)$$

Where C_0 (mg/l) represents the initial concentration of (MB) dye, C_t (mg/l) is the concentration of the pollutant at time t, and Kapp: represents the rate constant (min^{-1}).

4. Results and Discussion

4.1 Structural proprieties

XRD Patterns

The X-ray diffraction patterns of $NiFe_2O_4$ nanoparticles obtained from both precursors are represented in (Fig 1). The Bragg reflections were observed as high-intensity peaks and sharp diffractions without any amorphous phase. It can be observed that the position and the relative peaks intensity correspond well to the standard nickel ferrite $NiFe_2O_4$ according to the JCPDS No. 54-0964 which confirms the structure [43, 44]. For both cases, the XRD model shows the characteristic peaks at 2θ = 30.24°, 35.57°, 37,14°, 45.46°, 47.92°, 53.74°, 57.18°, 62.80°, 66.25°, and 75.30° correspond respectively to (220), (311), (222), (400), (411), (422), (511),

(440), (531) and (444) respectively. [23, 45, 46]. This result explains that all these peaks can be perfectly fit with cubic spinel structure under space group symmetry Fd-3m [47]. The XRD patterns show also some other peaks associated to impurities more in NFSP, these impurities are due to the presence of α-Fe_2O_3 phase [48]. These obtained results show that the use of $FeCl_2$ allows for giving a smaller crystallite size and better purity phase than $FeSO_4$ which is probably due to the good compatibility, better solubility, and excellent crystallinity growth of chloride precursor between ($FeCl_2$/$Ni(NO_3)_2$) couple. Indeed, the electrostatic interactions between chloride and nitrate counter ions developed a better phase purity and compatibility than sulphate and nitrate counter ions. The interactions between each counter-ion and metal cation during the synthesis can create a definite supramolecular structure of $NiFe_2O_4$ which can lead to considerable variations in structural growth and phase purity in both samples [49]. The X-ray density of $NiFe_2O_4$ was calculated using the equation, $\rho_x = 8M / Na^3$. Where M is the molecular weight of $NiFe_2O_4$ (234.38 g/mol), N_a is the Avogadro constant and a_0 is the lattice parameter [39, 50]. (Table.1S) represent Phase space group, $2\theta_{hkl}$, ρ_x, X-ray Density, d_{hkl}, Lattice parameter, $a_{0,}$ FWHM and crystallite size of both samples.

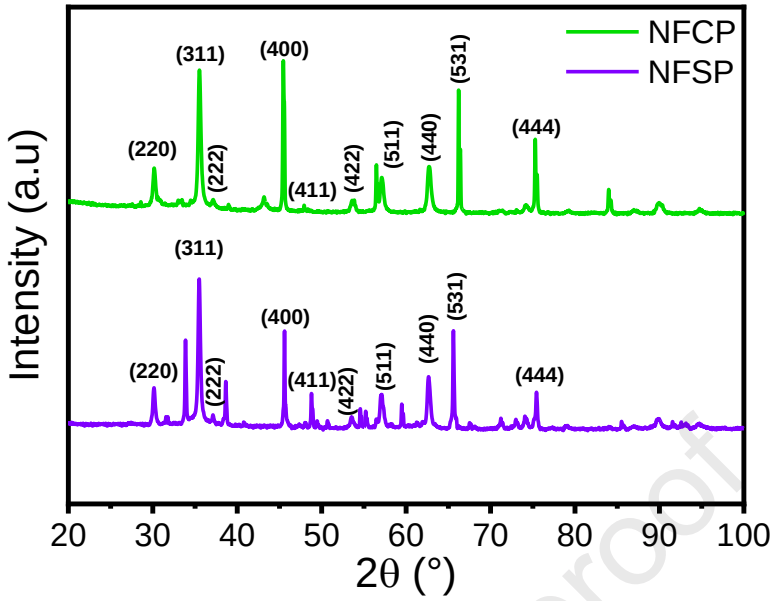

Fig. 1 XRD patterns of obtained samples

4.2 Crystallite size determination

4.2.1 Scherrer method.

The FWHM value of the characteristic peak (311) was taken to calculate the crystallite size of $NiFe_2O_4$ nanoparticles based on the literature [50] (Table.1S) to calculate the crystallite size of $NiFe_2O_4$ nanoparticles we applied Scherer's equation described in (Eq. (2)) [51, 52].

$$D = k.\lambda/\beta.Cos\theta \quad (2)$$

$$\beta = \beta^2_{meas} - \beta^2_{Inst} \quad (3)$$

$$cos\theta = k.\lambda/D.(1/\beta) \quad (4)$$

Where D is the crystallite size in (nm), λ is the wavelength of the X-ray wavelength (λCuKα = 0.1540598 nm), K is the shape factor (K = 0.9), β is the (FWHM) of the characteristic peak (in radians) and θ is the Bragg diffraction angle for hkl plane, β_{hkl} is Full Width at Half Maximum for every peak) β_{inst} is Full Width at Half Maximum for the instrumental, and β_{meas} is Full Width at Half Maximum of the measured sample.

4.2.2 Williamson-Hall Method

The crystallite size (D) and lattice strain given by Eqt. (2) and (8) respectively can influence and contribute to the diffraction peak broadening [40]. which are explained in (Fig.1S). W–H method depends on (tanθ) and does not follow (1/cosθ) as in the Scherrer formula, this difference provides for a separation of reflection broadening when both microstructural elements of small crystallite size and microstrain are shown together [51, 53, 54]. The θ depend on both effects of size and strain broadening in the analysis of Williamson and Hall. Addition of the Scherrer equation and ε results in the next equations. Bragg reflection can be described as results:

$$\beta_{hkl} = \beta s + \beta_D \quad (5)$$

β_{hkl} expresses (FWHM) in radiant. The W-H ensure the strain stay uniform during the crystallographic trajectory, is mentioned by β_{hkl}.

$$\beta_{hkl} = (k\lambda/D\cos\theta) + 4\varepsilon \tan\theta \quad (6)$$

Replacing Eq. (6) produces

$$\beta_{hkl} = (k\lambda/D) + 4\varepsilon\sin\theta \quad (7)$$

$$\varepsilon = \beta s/4 \tan\theta \quad (8)$$

Eq (7) represents the UDM where the strain was considered to be uniform in all the crystallographic directions, thus considering the isotropic nature of the crystal where all the material characteristics are independent of the direction measured [55] with respect (βcosθ) was plotted to (4sinθ) for the selected orientation peaks of $NiFe_2O_4$ with the cubic phase, consequently, the slope and y-intersect of the fitted line describe the strain and particle size respectively[53]. The plots showed a direct proportion between the crystallite size and strain value due to the compressive stresses. The UDM analysis results are shown in (Fig.1S); the details in (Table.2S) represent the Scherrer, UDM, and SSP methods of calculating the size crystallites of both catalysts.

4.2.3 Size-Strain Plot Method

The line broadening was isotropic proved using the Williamson-Hall plot, the diffracting domains were isotropic due to microstrain combination. The "size-strain plot" (SSP) can give the size-strain parameters. This is the advantage that little attraction is presented to data from reflections at elevated angles. In this analysis, it is supposed that the profile is described as "strain profile" by a Gaussian function and the "crystallite size" by the Lorentzian process [56] Subscribed equation.

$$(d_{hkl}\,\beta_{hkl}\cos\theta)^2 = \frac{k}{D}\,(d^2_{hkl}\,\beta\cos\theta) + \left(\frac{\varepsilon}{2}\right)^2 \qquad (9)$$

where *k* is a constant, shape of the particles for spherical particles it is given as 3/4. In Fig. 2 $(d^2_{hkl}\,\beta\cos\theta)$ were taken in x-axis and $(d_{hkl}\,\beta_{hkl}\cos\theta)^2$ on y-axis. The strain was given using the root of the y-intercept and slope linearly fitted data to calculate the particle size.

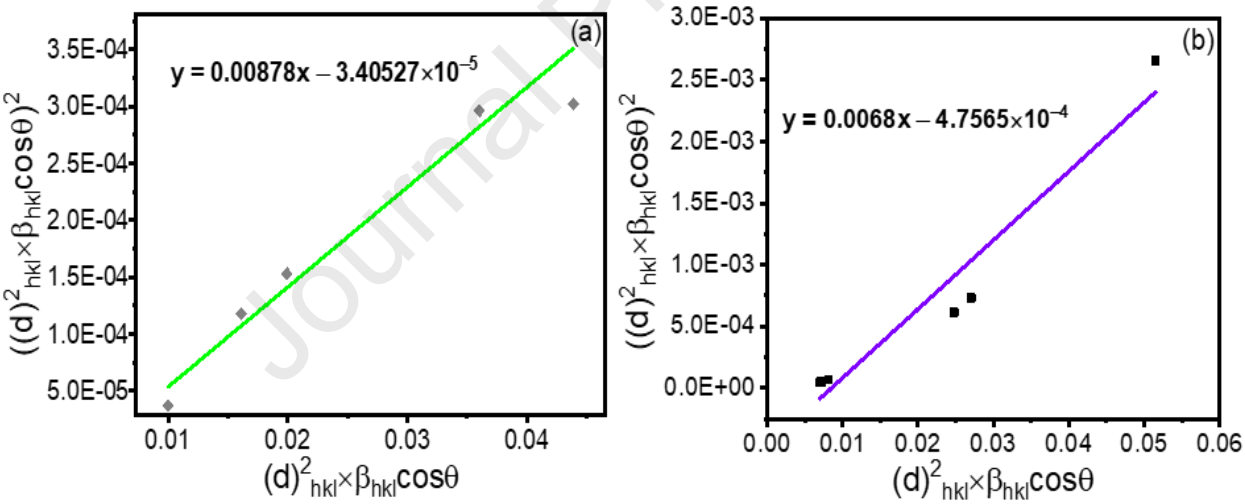

Fig.2. The SSP plot of NFCP (a) NFSP (b) to the particle size is achieved from the slop of the liner fitted data and the root of y-intercept gives the strain.

4.3 XPS analysis

To analyse the elemental composition of the material surface, an X-ray photoelectron spectroscopy analysis was performed to the best catalyst "NFCP". The XPS survey represented in (Fig. 3) confirms the appearance of nickel, iron, carbon, and oxygen in the composition. The appearance of Fe2p, Ni2p, and O1s region spectra are given in Fig .3 (b, c, and d respectively).

A C1s peak is also observed in the XPS survey spectrum, the presence of this peak is because of the reaction was carried out under normal conditions, which causes the presence of CO_2 on the surface of the material, this case is commonly encountered in the study of the structural properties of metal oxides. Two important peaks were observed in the Fe2p spectrum at 710.2 and 724.2 eV which are attributed to Fe2p3/2 and Fe2p1/2 respectively [57, 58]. Another peak at 55 eV belongs also to the iron atom and is attributed to Fe3p [46]. The Ni2p spectrum show four peaks, two intense peaks of $Ni2p_{1/2}$ and $Ni2p_{3/2}$ at 872.9eV and 855.4 eV respectively and two satellites at 878.1 eV and 862 eV corresponding to Ni $2p_{1/2}$ and Ni $2p_{3/2}$ respectively indicating the co-existence of Ni^{2+}/Ni^{3+} in the catalyst [59, 60]. O1s spectra present also two peaks, the first one located at 531 eV and another peak at 529.6 eV, the two peaks are attributed to oxygen bonds with the metal in the metal oxides [61-63]. All values are identical to those obtained in the literature which confirms the formation of $NiFe_2O_4$ Nanoparticle.

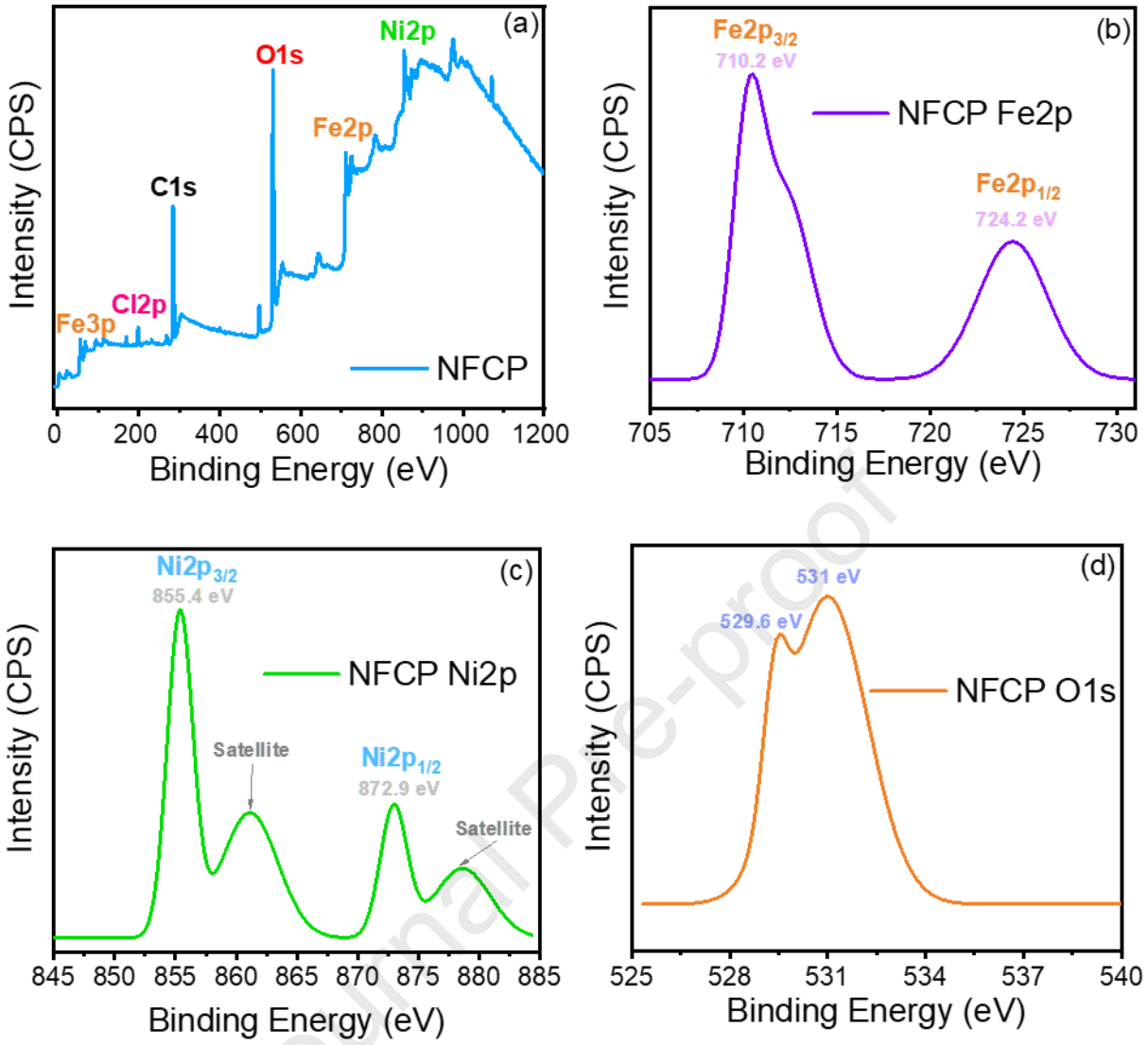

Fig 3. XPS spectra of: (a) NFCP survey, (b) NFCP Fe2p, (c) NFCP Ni2p, (d) NFCP O1s.

4.4 FTIR analysis

In order to show the difference in the functional groups for both $NiFe_2O_4$ materials, the FTIR spectra were carried out for the obtained samples and regrouped in the Fig. 4. The absorption band appeared between 3000–3450 cm^{-1} is attributed to the O−H stretching vibration of the physisorbed water on the surface of the materials which confirm the hydrophilic nature of the nickel ferrite nanoparticles [12, 64] The bands in the region between1200–1700 cm^{-1} are assigned to the stretching vibration of the C=O function belonging to the CO_2 as the analysis is performed in a non-inert atmosphere and to the bending vibration of water O–H groups.[42] The stretching bond of the metal-oxide groups Fe−O groups in octahedral position and the

Ni−O groups in tetrahedral position are observed at 474 cm^{-1} and 570 cm^{-1} respectively [65]. The FT-IR spectrum also shows a similar structure between NFCP and NFSP with the same bands, which proves that the choice of counter ion does not change the structural properties on the functional groups of the material.

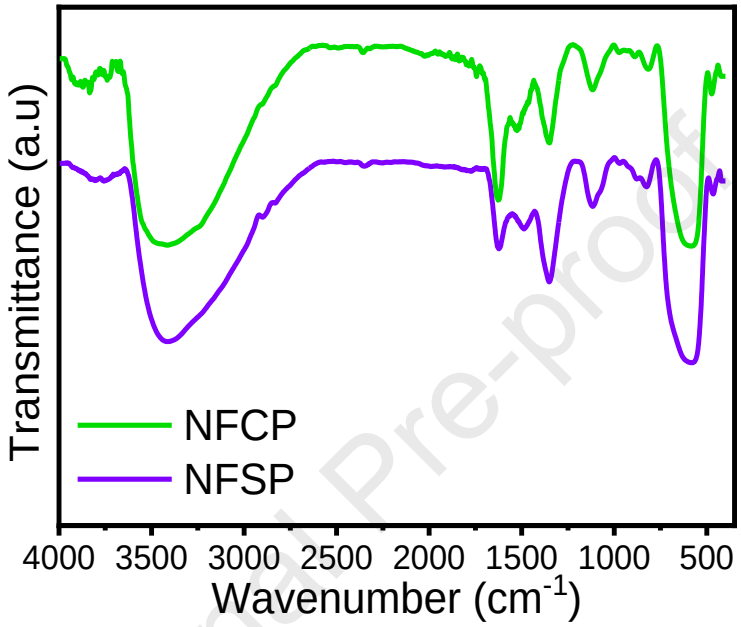

Fig. 4. FTIR spectra of both $NiFe_2O_4$ materials

4.5 SEM/EDS analysis

The morphology of both metal's oxide nanoparticles was analysed using SEM images and was presented in (Fig.5). The two samples show a very similar morphology, the morphology observed for both nickel ferrite nanoparticles are spherical with homogenous size and an aggregated tendency uniformly distributed, which is due to its magnetic nature. This morphology is identical to that found in the literature which reinforces the results observed by XRD and XPS [20, 27, 66]. A significant difference is also observed in the SEM images between the two samples, where the NFCP shows a clearly smaller size see (Table 1S and 2S) and is more homogenous than that observed in the NFSP, this is probably due to the better phase purity

(XRD result) and good compatibility between cation and their counter ions observed in the chloride phase.

The EDS analysis of both samples exposed in the Fig.5. shows the presence of all components of the $NiFe_2O_4$ molecule, which is in accordance with the results obtained by XPS analysis. The figure shows also a higher percentage of the Ni in the NFCP obtained from the chloride phase compared to the NFSP, this observation confirms the results found in the XRD analysis which indicated that the NFCP is purer than its alternative. Another fact can be observed from the figure, the EDS mapping images of both samples reveal that all composition atoms of these nanoparticles are well dispersed and there is no area where an atom are not present which confirm the effectiveness of the operating method used for the preparation of the materials.

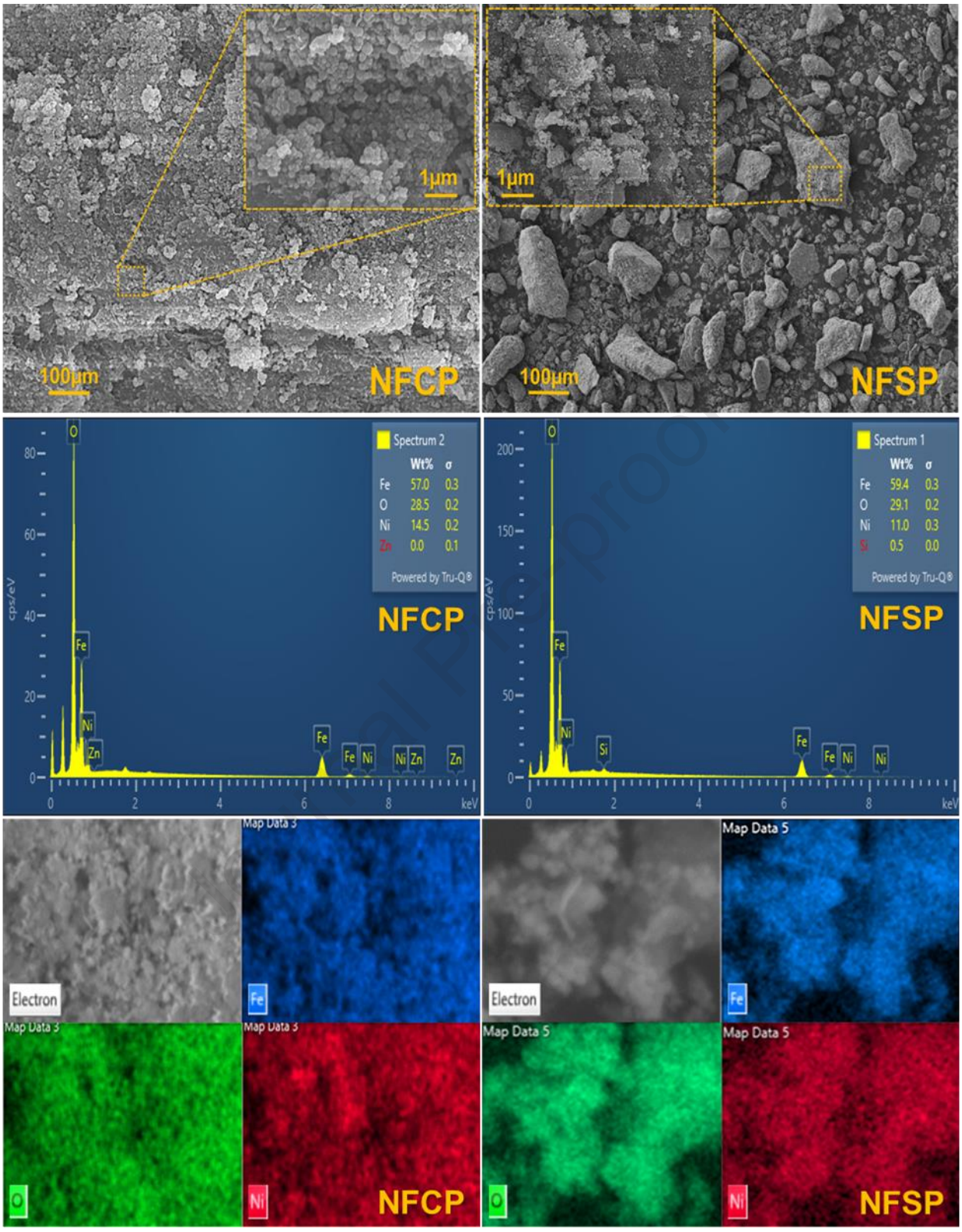

Fig. 5. SEM and EDS mapping images of both samples.

4.6 Vibrating sample magnetometer (VSM)

The magnetic hysteresis loops of the best catalyst (NFCP) got at room temperature given in the magnetic hysteresis loops of the best catalyst (NFCP) got at room temperature given in (Fig. 6). The couple showed an important saturation magnetization with low coercivity this feature shows a ferromagnetic behaviour at room temperature which exhibits uniform morphology and high crystallinity of sample which explain the material is soft ferromagnetic [32, 67]. The combination of metal cation in the tetrahedral and octahedral position can affect the magnetic properties of the sample [50, 68]. Depending on the various synthesis protocols the values of Ms change [69]. Following the co-precipitation technique, the described saturation magnetization values of $NiFe_2O_4$ in the papers were varied to be 50 emu g/1 [70], 47.4emu g/1 [71], 16.71emu g/l [72] and 8.9 emu g/l [44] From the M–H curve the catalyst NFCP Presents a high value of (Ms) with a small particle size this high permeability magnetization of the sample was enough for magnetic separation. The small particle size decreases the barrier or anisotropy energy [73]. The hysteresis loop of NFCP catalyst exhibit the values of saturation magnetization (Ms), remanent magnetization (Mr), coercivity (Hc), squareness ratio (Mr/Ms) and magnetic moment (nB) values depicted in (Table 1) similar results obtained by previous publication [74].

Table 1: Different magnetic parameters calculated from M-H curve of NFCP catalyst.

Sample	Ms (emu/g)	Mr (emu/g)	Hc (Oe)	Mr/Ms	nB(exp)	nB (neel)	D(nm)
NFCP	67.79	10.11	93.41	0.148	2.869	2.90	29

We determine the magnetic moment in Bohr magneton (μB) below [50, 75] (see Table 1).

$$N_b\,(exp) = \frac{Ms \times M}{5585} \qquad (10)$$

Where (Ms) is saturation magnetization and (M) is the molecular weight. According to Neel's theory, using the relation shown in (Eq.12) we calculated the net magnetic moment by the reversely aligned magnetic moments on tetrahedral and octahedral sites.

N_B (neel) = $M_B - M_A$ (11)

$Hc = \frac{0,96.k}{5585}$ (12)

The ratio of Mr/Ms represents the squareness of the hysteresis loop, It has been written that the squareness ratio at or higher than 0.5 means that the element is in a single magnetic domain and under 0.5 can be attached to the development of a multidomain structure [50, 76]. The determined value of the squareness ratio of the samples below 0.5 clearly understands that the sample synthesized by this method are multi-domain in the constitution. The squareness ratio for the sample fabricated via was found to be 0.152 and for SPM the typical value of Mr/Ms is << 0.01 [77]. Bohr magneton (nB) of the synthesized sample is less than the calculated theoretical value of 2.869 for experimental and 2.9 for theoretical. This difference may be because of less inversion degree in the obtained material [78].

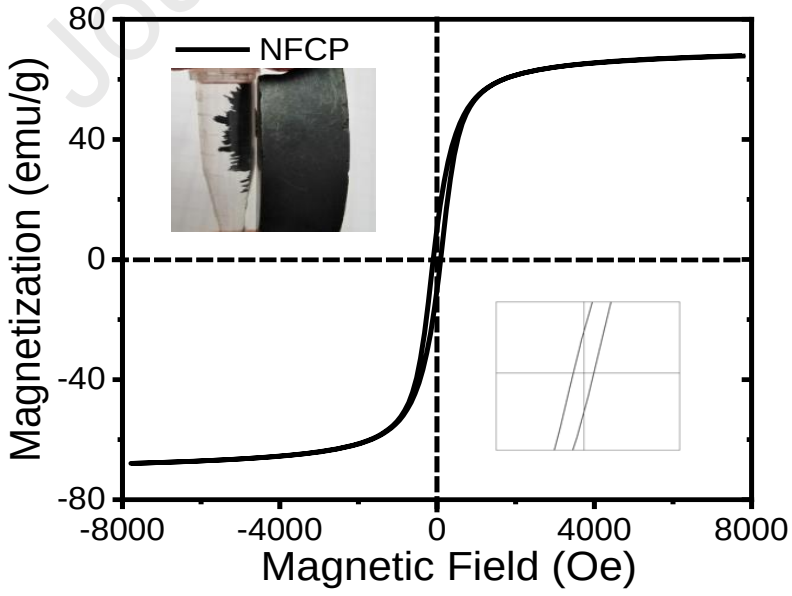

Fig. 6. Vibrating sample magnetometer (VSM) analysis of NFCP.

4.7 Zeta Potential

The zeta potential was carried out to determine the surface charge in the pH range from 3 to 11 and to explain the affinity between the catalyst and the organic dyes MB and OG. The obtained results of NFCP and NFSP are shown in Fig.7. Both samples showed a very similar zeta potential to the literature which confirms the results obtained [79], [80]. From the figure it is observed that there is a slight difference in the surface charge between NFCP and NFSP, where NFCP shows a more negative surface over the whole pH range, this surface charge shift is due to the difference in electronegativity between the counter ions $2Cl^-$ and $SO4^{2-}$. This shift explains also the better affinity between NFCP and methylene blue as well as its better catalytic activity compared to NFSP which proves the importance of choosing the counter ion used for the $NiFe_2O_4$ synthesis. Fig.7 shows also surface positivity until about pH = 6.79 and pH = 6.91 for NFCP and NFSP respectively, then the surface becomes negative for the rest of the range.

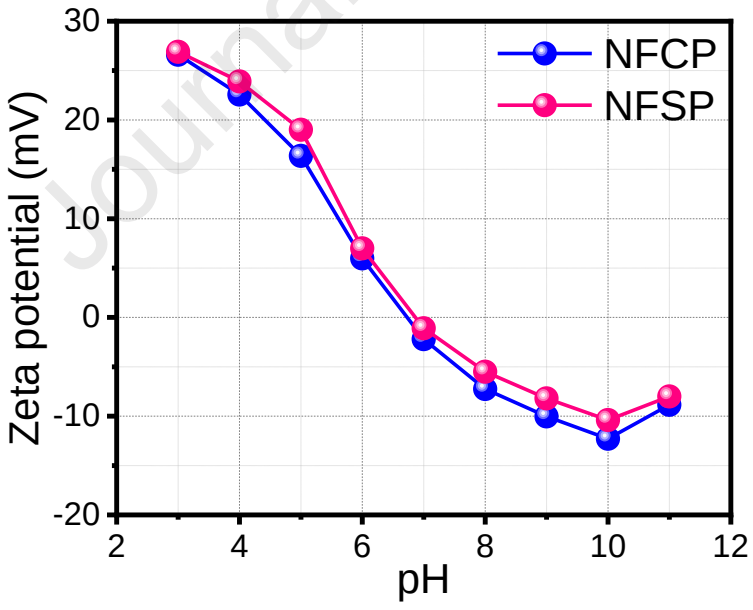

Fig. 7. Zeta potential of both samples at different value of pH.

5- Catalytic reduction study of organic dyes

To evaluate the catalytic activity, a model reaction of reduction of MB and OG dyes was carried out in the presence of two different catalysts of $NiFe_2O_4$. Since the character of the nanoparticle

and their loading content can ensure the reduction of organic dyes. Much research proves the (MB) dye reduction in the existence of a catalyst and $NaBH_4$ conducts to the conversion of leuco-MB which is colourless and less toxic than (MB) dye [81, 82]. Without the use of a catalyst the reaction of hydrogenation of organic pollutants cannot conduct any conversion. Moreover, Baye et al [83] proved that the addition of $NaBH_4$ solution to a hazardous materials "4-nitrophenol" doesn't conduct any change after 60 h of reaction time, upon adding catalyst, 4-nitrophenol was directly converted into 4-aminophenol [84]. To confirm the best catalyst in terms of effectiveness using a catalyst and without $NaBH_4$, an adsorption test was also carried out, the results exposed in (Fig.8a and 8b) show that neither NFCP nor NFSP catalysts have an adsorption capacity against the (MB) dye even after 15 min of contact between catalysts and (MB) dye. The plot of C_t/C_0 as a function of the reaction time (Fig.9.) permit assuming some practical detail on the catalytic manner and selectivity of the catalyst (Table 2). The figures 8c, 8d and 2S show that all catalysts have a great activity via the reduction of the both dyes. This efficiency of both catalysts in the presence of $NaBH_4$ toward the organic dyes is due to their many actives sites which allow the fixation of a large amount of MB or OG molecules towards active sites followed by the leuco-methylene Blue release for the methylene blue dye or the sodium 8-amino-7-hydroxynaphthalene-1,3-disulfonate and aniline release in case of orange G molecule. NFCP exhibit better catalytic activity and faster than NFSP perhaps to the complete formation of NFCP catalyst, this is due to its purest phase, higher amount of Nickel atom, smallest crystallite size and its higher degree of dispersion see (XRD result, Table 1S, and SEM/EDS image). Fig.8c and 8d show that the reduction time of (MB) dye was 8 min using the catalyst NFCP while NFSP was approximately 11 min, while for the orange G dye the required time for total reduction were 4 minute for both catalysts with a slight superiority of the NFCP as shown in the Fig.2S (See supplementary data). This different time of reduction between the catalysts against the same pollutant and toward both of them is related to the choice

of counter ion, which has led to the difference in nanoparticles sizes between both catalysts and to the difference in the surface negativity. These two parameters are the keys to this excellent photoreduction activity meaning that the size of the nanoparticle is directly linked to the activity of the material, when the size is smaller, the efficiency is higher [12]. The second parameter is the material surface charge, when the surface of the material is negative; it allows a better affinity with the MB dye, which is a cationic dye, so the more negative the surface, the more affinity as well the activity is better. This second parameter also explains why the degradation of orange G was faster than the degradation of methylene blue. Indeed, by observing the zeta potential of both materials we can see that their surface charge in a pH range between 6-7 (the pH range of water) is positive, and since orange G is known to be an anionic dye, the electrostatic interactions between the material and the organic molecule of the pollutant are more favourable with orange G than with MB. This process can be clarified by the redox reaction and the move of electrons to the surface of the catalyst. Firstly, the BH_4^- ions in the reaction conduct to the generation of electron close to the $NiFe_2O_4$ metal nanoparticles following by the fixation of the organic dye (MB/OG) via electrostatic interactions and ensures the degradation activity, the resulting product are then desorbed and released (scheme 1) [85-87]. The reduction of MB results in the formation of leucomethylene blue (LMB) which is a colorless product well known to be less toxic than the organic dye MB; while for the photocatalytic reduction of the azo dye (OG), a formation of hydrazine as an intermediate product are firstly obtained before the cleavage of this bond into simple amine derivatives (the sodium 8-amino-7-hydroxynaphthalene-1,3-disulfonate and aniline). Nickel amount in the catalyst and the high synergy between the Nickel and Iron metals is also a very important parameter that can influence the reduction efficiency, this conclusion can be taken by observing the EDS picture where NFCP showed a higher amount of the Nickel atoms in the molecule and by linking this result with the better catalytic activity of this catalyst. Indeed, in our precious

work we showed that the content and dispersion of the metallic nanoparticles can have a great impact on the reduction time, i.e. more the amount of the nanoparticle and their dispersion in the matrix are higher and better, the time needed for total degradation of the organic dye is lower [88].

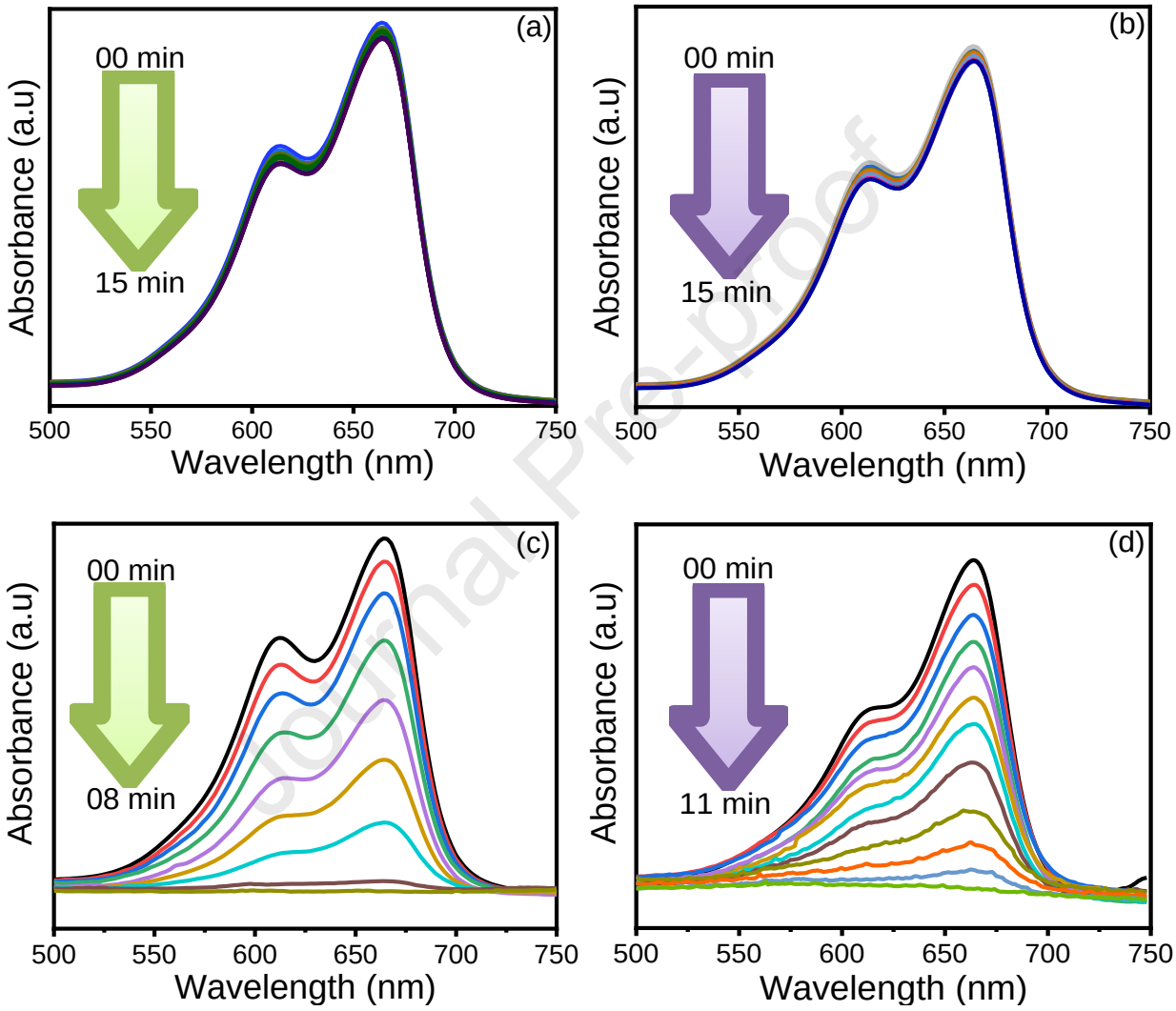

Fig. 8. UV-vis of MB dye during its (a) NFCP, (b) NFSP absorption without $NabH_4$ (c) NFCP, (d) NFSP reduction with the presence of catalyst and $NaBH_4$.

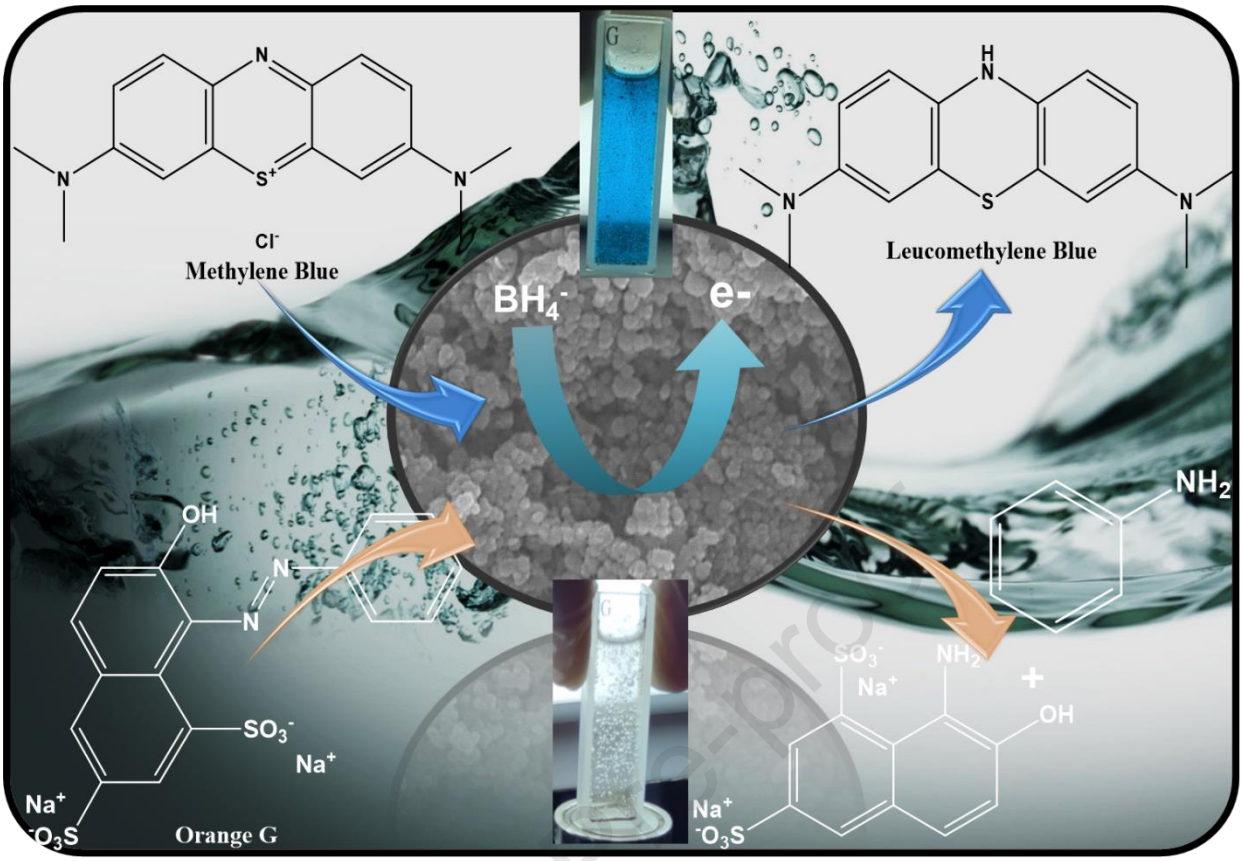

Scheme 1. Schematic illustration of the reduction of MB and OG by the $NiFe_2O_4$ in the presence of $NaBH_4$.

From Fig. 10, it can be observed that among both samples the K_{app} value for NFCP is 1.3804 min^{-1} which is higher than NFSP 0.4421 min^{-1} against MB dye (Table 2). The resulting K_{app} values of the catalysts against OG where observed from the Fig.2S, the NFCP showed also a superiority in the reduction of the anionic dye Orange G compared to the NFSP. The obtained values were 0.4514 min^{-1} and 0.4227 min^{-1} for NFCP and NFSP respectively (Table 2). Where the rate constant K_{app} was calculated from pseudo-first-order kinetics as described in Eq (1). The degradation of (MB) at the first started slow rate but later the reaction was increased swiftly. It can also be observed that for both catalysts there is an induction period, this induction period (t_0) is a delay time during the MB dye reduction where diverse atoms of the surface of the catalyst keep ready before the start of the reaction [89]. The atoms of the surface of the catalyst expose their active sites in terms of faces, edges, or corners these conduct an increase in the rate

of reaction and the delay time were is considered positive [90]. This period took usually between a few second to hours in some cases. When the delay of induction period of NFCP and NFSP was 4 and 5 min respectively (Fig.10.). For the OG dye, no induction period was observed this is mainly due to the favourable electrostatic interactions between the anionic dye and the positive surface charge of the catalysts allowing a very fast photocatalytic reduction (04 min for both materials).

Table 2. Rate constant of catalysts used for reduction of MB and OG.

Dye	Catalyst	K_{app} (min^{-1})	K^a ($min^{-1}.mg^{-1}$)
MB	NFCP	1.3804	0.6902
	NFSP	0.4421	0.2211
OG	NFCP	0.4514	0.2257
	NFSP	0.4227	0.2114

[a] The apparent rate constant normalized by the effective weight of the catalyst.

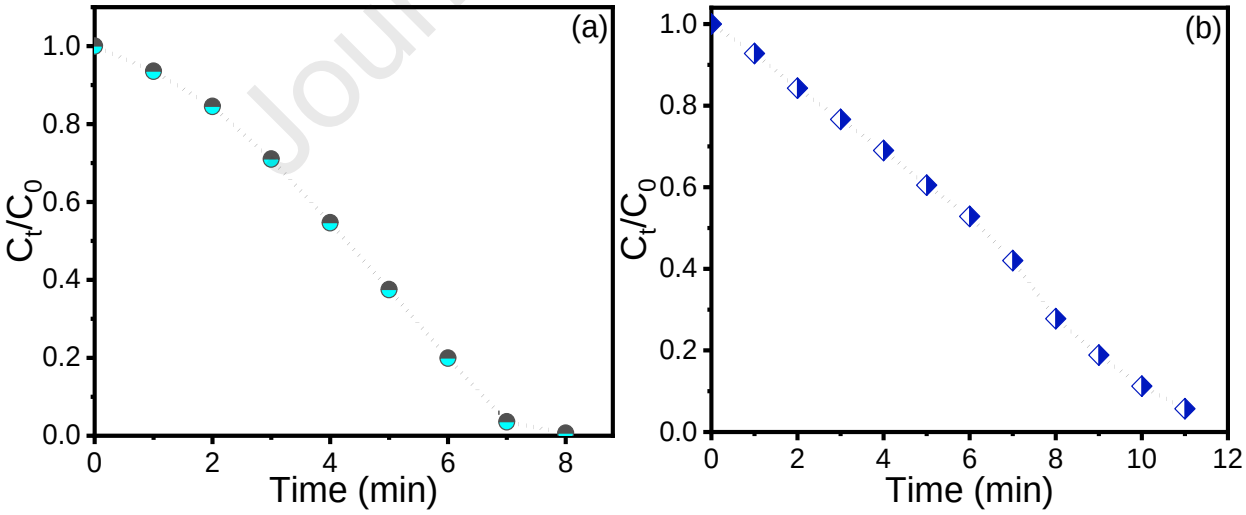

Fig.9. Conversion of MB dye using catalyst NFCP (a) and NFSP (b) depending on reaction time (min).

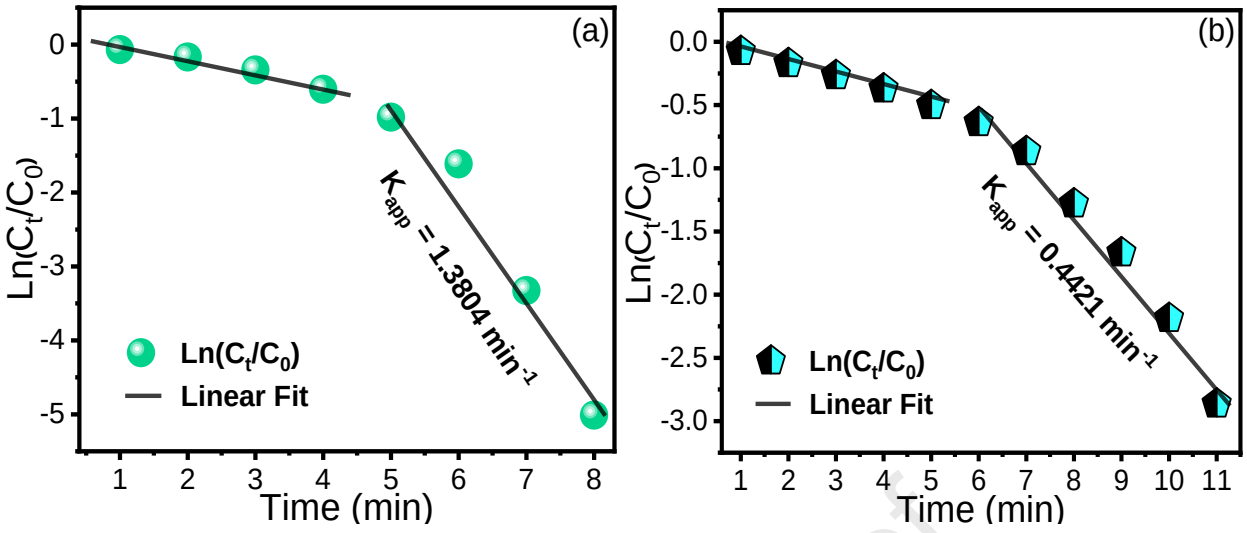

Fig. 10. Plots of ln [Ct\C0] versus time for the reduction of MB dye using catalyst NFCP (a) and NFSP (b).

A comparative study was carried out between our photocatalysts and other materials already published previously in the literature and to better distinguish the difference, the results have been grouped in (Table 3). NFCP shows a good catalytic activity toward the MB dye compared to the NFSP and much other noble metal basis photocatalyst (such as Ag or Au). It was found that the apparent rate constant normalized by the effective weight of the catalyst (K) was 0.6902 $min^{-1}.mg^{-1}$ For NFCP and 0.2211 $min^{-1}.mg^{-1}$ for NFSP. The concentration of MB dye and the mass of the catalyst must be taken into account during the comparison. Indeed, the concentration used of the pollutant is quite high, while the mass of the catalyst is low. This proves once again the efficiency of the NFCP material as well as NFSP and by taking into consideration their low cost we can affirm that they are excellent catalysts.

Table 3. Comparative study via the reduction of MB dye between our best catalyst and those carried out in the literature.

Catalyst	**Catalyst amont (mg)**	**[Polluant] (mM)**	**k_{app} (min^{-1})**	**K (min^{-1} .mg^{-1})**	**Ref**
Ni-Y	3	0.01	0.3	0.100	[88]
Co/Zeolite@ALG	4	0.6	1.40	0.35	[41]
Au@polypyrrole/Fe_3O_4	2	0.06	0.26	0.13	[91]
Fe_3O_4@Polydopamine-Ag	5	0.1	0.43	0.086	[92]
Au@TiO_2	2	0.04	0.156	0.078	[93]
Au@TA-GH	2	0.03	0.310	0.155	[94]
Ag/PSNM-3	2	0.03	0.13	0.065	[95]
Ag- Fe_3O_4	5	0.16	0.48	0.096	[96]
MIL-101(Cr)/CuNPs	3	0.6	0.50	0.167	[97]
M(1)@MIL-101/CA	4.8	0.6	0.962	0.200	[17]
NFCP	**2**	**0.6**	**1.3804**	**0.6902**	**This Work**

Catalysts recyclability

The most important ability of these nanoparticles is the reusability without losing their activity, in this study the reuse efficiency of our best catalyst "NFCP" was studied. After the total degradation, an external magnet was used easily to separate the catalyst from the solution, after washing with distilled water the catalyst was reused again. After each manipulation, the activity of the catalyst was estimated by the UV-Vis spectrophotometer. The results are exposed in (Fig.11). This manipulation was repeated 5 times to prove that this photocatalyst has a stable activity. Effectively, the results show that the catalyst capacity in the reduction of the organic dye (MB) has not decreased after five times which is very promising.

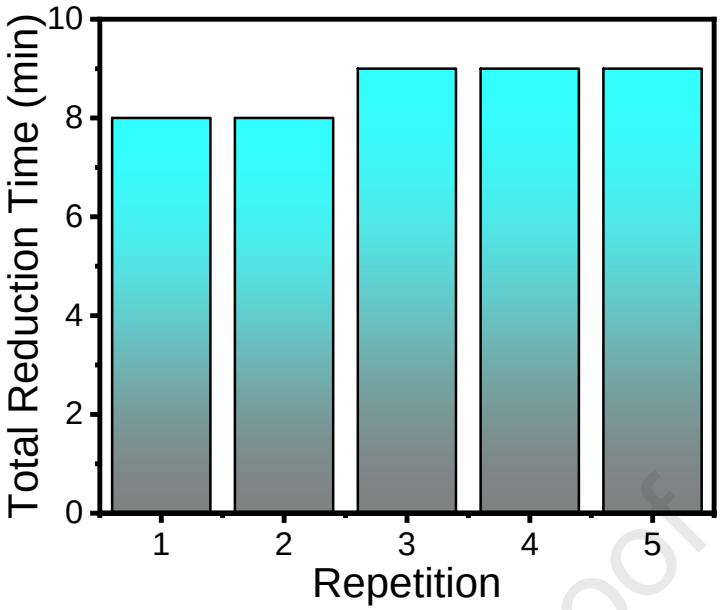

Fig.11. Reuse of the NFCP catalyst during five consecutive cycles via the reduction of MB dye.

5. Conclusion

In the current study, the synthesis of $NiFe_2O_4$ via co-precipitation method was carried out with different counter ions named NFCP and NFSP, A comparative study of the structural and morphological properties as well as its photoreduction activity toward the MB dye was performed. The XRD pattern confirms the desired structure and the cubic phase structure with space group Fd-3m, the crystallite size calculated using Scherer's formula, W-H plot, and SSP method. The phase purity, crystallite size, morphology and the surface charge properties of the $NiFe_2O_4$ powders varied upon changing the counter ion. The adsorption capacity of the two catalysts was evaluated and it can be seen that no adsorption took place even when the material remained in contact with the dye for a long period. The kinetics of degradation using $NaBH_4$ and catalyst was investigated in this research. Both photocatalysts exhibited a high photoreduction activity towards the reduction of the MB and OG dye, the best performance was obtained for the NFCP catalyst having the smallest size according to the purest phase due to the better formation of $NiFe_2O_4$ and compatibility between their counter ions. An induction period

was only observed in the reduction of (MB) dye. The highest rate constant k_{app} was found 1.3804 min^{-1} and 0.4514 min^{-1} for (MB) and (OG) dye respectively corresponding to the best catalyst. Finally, we evaluated the recyclability of the catalyst the performance of these catalysts gives satisfactory results during their reuse.

Supplementary Data

A supporting file was uploaded separately.

Declaration of competing interest

The authors declare that they have no conflict of interest.

Author statement

Cheikh Reda Bernaoui: Conceptualization, Validation, Methodology, Visualization, Writing- original draft, Software, Investigation, Data Curation. **Abdelaziz Bendraoua:** Writing - review & editing, Project administration. **Farouk Zaoui:** Writing- original draft, Review & editing, Software, Conceptualization, Visualization, Validation, Investigation, Data Curation, Project administration, Resources. **Juan Jesús Gallardo:** Writing - Review & Editing. **Javier Navas:** Writing - review & editing, Resources. **Rafik Abdelkrim Boudia:** Formal analysis, Writing - review & editing. **Houria Djediai:** Writing - Review & Editing. **Nor el Houda Goual:** Writing - Review & Editing. **Mehdi Adjdir:** Formal analysis, Writing - review & editing, Conceptualization.

Acknowledgment

The authors thank the DGRSDT, Algeria "Direction Générale de la Recherche Scientifique et du Développement Technologique" for funding this work.

References

1. Boughrara, L., et al., *New alginic acid derivatives ester for methylene blue dye adsorption: kinetic, isotherm, thermodynamic, and mechanism study.* International Journal of Biological Macromolecules, 2022. **205**: p. 651-663.
2. Bencherif, S.D., et al., *Synthesis, Characterization and Photocatalytic Performance of Calcined ZnCr-Layered Double Hydroxides.* Nanomaterials, 2021. **11**(11): p. 3051.

3. Boughrara, L., et al., *Removal of Zn (II) and Ni (II) heavy metal ions by new alginic acid-ester derivatives materials.* Carbohydrate Polymers, 2021. **272**: p. 118439.
4. Tatarchuk, T., et al., *Green and ecofriendly materials for the remediation of inorganic and organic pollutants in water.* A new generation material graphene: Applications in water technology, 2019: p. 69-110.
5. Tatarchuk, T., et al., *Green synthesis, structure, cations distribution and bonding characteristics of superparamagnetic cobalt-zinc ferrites nanoparticles for Pb (II) adsorption and magnetic hyperthermia applications.* Journal of Molecular Liquids, 2021. **328**: p. 115375.
6. Tatarchuk, T., et al., *Photocatalytic degradation of dyes using rutile TiO2 synthesized by reverse micelle and low temperature methods: real-time monitoring of the degradation kinetics.* Journal of Molecular Liquids, 2021. **342**: p. 117407.
7. Kumar, A., et al., *Accelerated charge transfer in well-designed S-scheme Fe@ TiO2/Boron carbon nitride heterostructures for high performance tetracycline removal and selective photo-reduction of CO2 greenhouse gas into CH4 fuel.* Chemosphere, 2022. **287**: p. 132301.
8. Alimohammadi, P., et al., *Oriented growth of copper & nickel-impregnated δ-MnO2 nanofilaments anchored onto sulfur-doped biochar template as hybrid adsorbents for removing phenolic compounds by adsorption-oxidation process.* Chemical Engineering and Processing-Process Intensification, 2022. **176**: p. 108971.
9. Nejad, M.S. and H. Sheibani, *Super-efficient removal of arsenic and mercury ions from wastewater by nanoporous biochar-supported poly 2-aminothiophenol.* Journal of Environmental Chemical Engineering, 2022. **10**(3): p. 107363.
10. Shahabi Nejad, M. and H. Sheibani, *Architecture of chitosan chains with sulfur-doped carbon dots along with decorating CeO2 nanoparticles for the photocatalytic application.* Journal of Applied Polymer Science, 2022. **139**(16): p. 51983.
11. Aminzadeh, H., et al., *Assembly of CuO nanorods onto poly (glycidylmethacrylate)@ polyaniline core–shell microspheres: Photocatalytic degradation of paracetamol.* Applied Organometallic Chemistry, 2021. **35**(12): p. e6423.
12. Zaoui, F., et al., *Ultrasonic preparation of a new composite poly (GMA)@ Ru/TiO2@ Fe3O4: Application in the catalytic reduction of organic pollutants.* Materials Chemistry and Physics, 2021. **260**: p. 124146.
13. Reyes-Pérez, F., et al., *Visible-light-enhanced photocatalytic activity of totally inorganic halide-based perovskite.* ChemistrySelect, 2018. **3**(36): p. 10226-10235.
14. Zarei, M., et al., *g-C3N4 quantum dot decorated MoS2/Fe3O4 as a novel recoverable catalyst for photodegradation of organic pollutant under visible light.* Journal of Materials Science: Materials in Electronics, 2021. **32**(22): p. 26213-26231.
15. Benhadria, N., et al., *Catalytic reduction of methylene blue dye by copper oxide nanoparticles.* Journal of Cluster Science, 2022. **33**(1): p. 249-260.
16. Habeche, F., et al., *Recent advances on the preparation and catalytic applications of metal complexes supported-mesoporous silica MCM-41.* Journal of Inorganic and Organometallic Polymers and Materials, 2020: p. 1-24.
17. Hachemaoui, M., et al., *Improved Catalytic Activity of Composite Beads Calcium Alginate@ MIL-101@ Fe 3 O 4 Towards Reduction Toxic Organic Dyes.* Journal of Polymers and the Environment, 2021: p. 1-14.
18. Jankovský, O., et al., *Simple synthesis of free surface nanostructured spinel NiFe2O4 with a tunable particle size.* Journal of Alloys and Compounds, 2017. **723**: p. 58-63.
19. Lazarova, T., et al., *Influence of the type of fuel used for the solution combustion synthesis on the structure, morphology and magnetic properties of nanosized NiFe2O4.* Journal of Alloys and Compounds, 2017. **700**: p. 272-283.

20. Ahankar, H., A. Ramazani, and S.W. Joo, *Magnetic nickel ferrite nanoparticles as an efficient catalyst for the preparation of polyhydroquinoline derivatives under microwave irradiation in solvent-free conditions.* Research on Chemical Intermediates, 2016. **42**(3): p. 2487-2500.
21. Xue, J., et al., *Characterization and microwave absorption of spinel MFe2O4 (M= Mg, Mn, Zn) nanoparticles prepared by a facile oxidation-precipitation process.* Journal of Magnetism and Magnetic Materials, 2020. **514**: p. 167168.
22. Cherpin, C., et al., *Study of the Solid-State Synthesis of Nickel Ferrite (NiFe2O4) by X-ray Diffraction (XRD), Scanning Electron Microscopy (SEM) and Raman Spectroscopy.* Materials, 2021. **14**(10): p. 2557.
23. Li, X., et al., *Nanostructural and magnetic studies of virtually monodispersed NiFe 2 O 4 nanocrystals synthesized by a liquid–solid-solution assisted hydrothermal route.* Journal of Nanoparticle Research, 2012. **14**(3): p. 1-9.
24. Amiri, M., M. Salavati-Niasari, and A. Akbari, *Magnetic nanocarriers: evolution of spinel ferrites for medical applications.* Advances in colloid and interface science, 2019. **265**: p. 29-44.
25. Sutka, A., et al., *Comparison of photocatalytic activity for different co-precipitated spinel ferrites.* Research on Chemical Intermediates, 2015. **41**(12): p. 9439-9449.
26. Bahhar, S., et al., *Structural, magnetic, magnetocaloric effect and critical behaviour study of NiCeFeO4 spinel ferrite.* Solid State Communications, 2020. **322**: p. 114056.
27. Egizbek, K., et al., *Stability and cytotoxicity study of NiFe2O4 nanocomposites synthesized by co-precipitation and subsequent thermal annealing.* Ceramics International, 2020. **46**(10): p. 16548-16555.
28. Gorgizadeh, M., N. Azarpira, and N. Sattarahmady, *In vitro and in vivo tumor annihilation by near-infrared photothermal effect of a NiFe2O4/C nanocomposite.* Colloids and Surfaces B: Biointerfaces, 2018. **170**: p. 393-400.
29. Sivakumar, P., et al., *Synthesis and characterization of NiFe2O4 nanosheet via polymer assisted co-precipitation method.* Materials Letters, 2011. **65**(3): p. 483-485.
30. Kim, C.-K., et al., *Synthesis of Co-, Co-Zn and Ni-Zn ferrite powders by the microwave-hydrothermal method.* Materials Research Bulletin, 2001. **36**(12): p. 2241-2250.
31. Udhaya, P.A., T. Bessy, and M. Meena, *Antibacterial activity of nickel and magnesium substituted ferrite nanoparticles synthesized via self-combustion method.* Materials Today: Proceedings, 2019. **8**: p. 169-175.
32. Majid, F., et al., *Synthesis and characterization of NiFe2O4 ferrite: Sol–gel and hydrothermal synthesis routes effect on magnetic, structural and dielectric characteristics.* Materials Chemistry and Physics, 2021. **258**: p. 123888.
33. Sivakumar, P., et al., *Preparation and properties of nickel ferrite (NiFe2O4) nanoparticles via sol–gel auto-combustion method.* Materials Research Bulletin, 2011. **46**(12): p. 2204-2207.
34. Mahmoud, M.H., et al., *Synthesis of highly ordered 30 nm NiFe2O4 particles by the microwave-combustion method.* Journal of Magnetism and Magnetic Materials, 2014. **369**: p. 55-61.
35. Soumia, A., et al., *Fe3O4-alginate nanocomposite hydrogel beads material: One-pot preparation, release kinetics and antibacterial activity.* International Journal of Biological Macromolecules, 2020. **145**: p. 466-475.
36. Sk, I., et al., *Synthesis of gold and silver nanoparticles using Malva verticillata leaves extract: Study of gold nanoparticles catalysed reduction of nitro-Schiff bases and antibacterial activities of silver nanoparticles.* Current Research in Green and Sustainable Chemistry, 2020. **3**: p. 100006.

37. Valenzuela, R., *Magnetic ceramics Cambridge University Press Cambridge 10.1017*. CBO9780511600296, 1994.
38. Mantilla, J., et al., *Evidence of surface spin-glass behavior in NiFe2O4 nanoparticles determined using magnetic resonance technique.* Journal of Magnetism and Magnetic Materials, 2019. **476**: p. 392-397.
39. Tatarchuk, T., et al., *Synthesis, morphology, crystallite size and adsorption properties of nanostructured Mg–Zn ferrites with enhanced porous structure.* Journal of Alloys and Compounds, 2020. **819**: p. 152945.
40. Prabhu, Y.T., et al., *X-ray analysis by Williamson-Hall and size-strain plot methods of ZnO nanoparticles with fuel variation.* World Journal of Nano Science and Engineering, 2014. **2014**.
41. Mekki, A., et al., *Catalytic behavior and antibacterial/antifungal activities of new MNPs/zeolite@ alginate composite beads.* International Journal of Biological Macromolecules, 2022. **198**: p. 37-45.
42. Hachemaoui, M., et al., *Composites beads based on Fe3O4@ MCM-41 and calcium alginate for enhanced catalytic reduction of organic dyes.* International Journal of Biological Macromolecules, 2020. **164**: p. 468-479.
43. Patel, G., et al., *Rice husk derived nano-NiFe2O4@ CAGC-catalyzed direct oxidation of toluene to benzyl benzoate under visible LED light.* FlatChem, 2020. **21**: p. 100163.
44. Khorshidi, P., et al., *Adsorptive removal of mercury (II), copper (II), and lead (II) ions from aqueous solutions using glutathione-functionalized NiFe 2 O 4/graphene oxide composite.* Research on Chemical Intermediates, 2020. **46**(7): p. 3607-3627.
45. Dridi, R., et al., *Physical study on nife2o4/α-Fe2O3 composite-thin films for potential applications.* Surfaces and Interfaces, 2020. **21**: p. 100743.
46. Abdullah, B. and D. Tahir. *Analysis of structural properties of X-ray diffraction for composite copper-activated carbon by modified Williamson-Hall and size-strain plotting methods*. in *Journal of Physics: Conference Series*. 2018. IOP Publishing.
47. Tiwari, R., et al., *Structural and magnetic properties of tailored NiFe2O4 nanostructures synthesized using auto-combustion method.* Results in Physics, 2020. **16**: p. 102916.
48. Lin, W.-S., et al., *Shape effects of iron nanowires on hyperthermia treatment.* Journal of Nanomaterials, 2013. **2013**.
49. Tong, M. and X. Chen, *Modern Inorganic Synthetic Chemistry*, 2017, Elsevier BV: Amsterdam, The Netherlands.
50. Prabhakaran, T. and J. Hemalatha, *Chemical control on the size and properties of nano NiFe2O4 synthesized by sol–gel autocombustion method.* Ceramics International, 2014. **40**(2): p. 3315-3324.
51. Sen, S.K., et al., *Dy-doped MoO3 nanobelts synthesized via hydrothermal route: Influence of Dy contents on the structural, morphological and optical properties.* Journal of Alloys and Compounds, 2021. **876**: p. 160070.
52. Kim, J.-Y., et al., *Morphology modification of TiO 2 nanotubes by controlling the starting material crystallite size for chemical synthesis.* Journal of Nanoparticle Research, 2011. **13**(6): p. 2319-2327.
53. Zak, A.K., et al., *X-ray analysis of ZnO nanoparticles by Williamson–Hall and size–strain plot methods.* Solid State Sciences, 2011. **13**(1): p. 251-256.
54. Ramaraghavulu, R., et al., *Green synthesized AgNPs decorated on Ketjen black for enhanced catalytic dye degradation.* Research on Chemical Intermediates, 2021. **47**(2): p. 637-648.

55. Devesa, S., et al., *Williamson-hall analysis in estimation of crystallite size and lattice strain in Bi1. 34Fe0. 66Nb1. 34O6. 35 prepared by the sol-gel method.* Materials Science and Engineering: B, 2021. **263**: p. 114830.
56. Nye, J.F., *Physical properties of crystals: their representation by tensors and matrices*1985: Oxford university press.
57. Fang, Z., et al., *Bimetallic NiFe 2 O 4 synthesized via confined carburization in NiFe-MOFs for efficient oxygen evolution reaction.* Journal of Nanoparticle Research, 2018. **20**(4): p. 1-10.
58. Fominykh, K., et al., *Iron-doped nickel oxide nanocrystals as highly efficient electrocatalysts for alkaline water splitting.* ACS nano, 2015. **9**(5): p. 5180-5188.
59. Lu, X. and C. Zhao, *Electrodeposition of hierarchically structured three-dimensional nickel–iron electrodes for efficient oxygen evolution at high current densities.* Nature communications, 2015. **6**(1): p. 1-7.
60. Dupin, J.-C., et al., *Systematic XPS studies of metal oxides, hydroxides and peroxides.* Physical Chemistry Chemical Physics, 2000. **2**(6): p. 1319-1324.
61. Cai, Y.-Z., et al., *Tailoring rGO-NiFe2O4 hybrids to tune transport of electrons and ions for supercapacitor electrodes.* Journal of Alloys and Compounds, 2019. **811**: p. 152011.
62. Wang, X., et al., *Antimony selenide nanorods decorated on reduced graphene oxide with excellent electrochemical properties for Li-ion batteries.* Journal of The Electrochemical Society, 2017. **164**(13): p. A2922.
63. Yadav, R.S., et al., *Structural, magnetic, dielectric, and electrical properties of NiFe2O4 spinel ferrite nanoparticles prepared by honey-mediated sol-gel combustion.* Journal of Physics and Chemistry of Solids, 2017. **107**: p. 150-161.
64. Zaoui, F., et al., *Ultrasonic preparation of new nanocomposites poly (GMA)@ amino-functionalized Fe3O4: structural, morphological and thermal properties.* Polymer Bulletin, 2022: p. 1-18.
65. Joshi, S., et al., *Structural, magnetic, dielectric and optical properties of nickel ferrite nanoparticles synthesized by co-precipitation method.* Journal of Molecular structure, 2014. **1076**: p. 55-62.
66. Talebi, R., *Preparation of nickel ferrite nanoparticles via a new route and study of their photocatalytic properties.* Journal of Materials Science: Materials in Electronics, 2017. **28**(5): p. 4058-4063.
67. Huo, J. and M. Wei, *Characterization and magnetic properties of nanocrystalline nickel ferrite synthesized by hydrothermal method.* Materials Letters, 2009. **63**(13-14): p. 1183-1184.
68. Golchinvafa, S. and S. Masoudpanah, *Magnetic and microwave absorption properties of FeNi3/NiFe2O4 composites synthesized by solution combustion method.* Journal of Alloys and Compounds, 2019. **787**: p. 390-396.
69. Narang, S.B. and K. Pubby, *Nickel spinel ferrites: A review.* Journal of Magnetism and Magnetic Materials, 2020: p. 167163.
70. Kombaiah, K., et al., *Catalytic studies of NiFe2O4 nanoparticles prepared by conventional and microwave combustion method.* Materials Chemistry and Physics, 2019. **221**: p. 11-28.
71. Iacovita, C., et al., *Saturation of specific absorption rate for soft and hard spinel ferrite nanoparticles synthesized by polyol process.* Magnetochemistry, 2020. **6**(2): p. 23.
72. Maleki, B., et al., *Silica-coated magnetic NiFe 2 O 4 nanoparticles-supported H 3 PW 12 O 40; synthesis, preparation, and application as an efficient, magnetic, green catalyst for one-pot synthesis of tetrahydrobenzo [b] pyran and pyrano [2, 3-c] pyrazole derivatives.* Research on Chemical Intermediates, 2016. **42**(4): p. 3071-3093.

73. Surya, R.M., et al., *One-pot Cajanus cajan (L.) Millsp. leaf extract-mediated preparation of MgFe2O4 nanoparticles: Optical, structural, morphological and particle size analyses.* Solid State Communications, 2021. **326**: p. 114170.
74. Sankaranarayanan, R., et al., *Effect of Ni 2+ and Fe 3+ Ion Concentrations on Structural, Optical, Magnetic, and Impedance Response of NiFe 2 O 4 Nanoparticles Prepared by Sol-Gel Process.* Journal of Superconductivity and Novel Magnetism, 2020. **33**(11): p. 3631-3642.
75. Kambale, R., *P. a. Shaikh, SS Kamble and YD Kolekar.* J. Alloys Compd, 2009. **478**: p. 599-603.
76. Baldi, G., et al., *Cobalt ferrite nanoparticles: The control of the particle size and surface state and their effects on magnetic properties.* Journal of Magnetism and Magnetic Materials, 2007. **311**(1): p. 10-16.
77. Theivasanthi, T. and M. Alagar, *Innovation of superparamagnetism in lead nanoparticles.* arXiv preprint arXiv:1402.1431, 2014.
78. Akhtar, M.N. and M.A. Khan, *Effect of rare earth doping on the structural and magnetic features of nanocrystalline spinel ferrites prepared via sol gel route.* Journal of Magnetism and Magnetic Materials, 2018. **460**: p. 268-277.
79. Iqubal, M.A. and R. Sharma, *Studies on interaction of ribonucleotides with zinc ferrite nanoparticles using spectroscopic and microscopic techniques.* Karbala International Journal of Modern Science, 2015. **1**(1): p. 49-59.
80. Ali Ahmad, M., et al., *Influence of morphology and crystallinity on surface reactivity of nanosized anatase TiO2 studied by adsorption techniques. 2. Solid–liquid interface.* The Journal of Physical Chemistry C, 2013. **117**(9): p. 4459-4469.
81. Bogireddy, N.K.R., K.K.H. Anand, and B.K. Mandal, *Gold nanoparticles—synthesis by Sterculia acuminata extract and its catalytic efficiency in alleviating different organic dyes.* Journal of Molecular Liquids, 2015. **211**: p. 868-875.
82. Narayanan, K.B. and H.H. Park, *Homogeneous catalytic activity of gold nanoparticles synthesized using turnip (Brassica rapa L.) leaf extract in the reductive degradation of cationic azo dye.* Korean Journal of Chemical Engineering, 2015. **32**(7): p. 1273-1277.
83. Baye, A.F., R. Appiah-Ntiamoah, and H. Kim, *Synergism of transition metal (Co, Ni, Fe, Mn) nanoparticles and "active support" Fe3O4@ C for catalytic reduction of 4-nitrophenol.* Science of The Total Environment, 2020. **712**: p. 135492.
84. Begum, R., et al., *Physical chemistry of catalytic reduction of nitroarenes using various nanocatalytic systems: past, present, and future.* Journal of Nanoparticle Research, 2016. **18**(8): p. 1-24.
85. Azad, U.P., V. Ganesan, and M. Pal, *Catalytic reduction of organic dyes at gold nanoparticles impregnated silica materials: influence of functional groups and surfactants.* Journal of Nanoparticle Research, 2011. **13**(9): p. 3951-3959.
86. Ghosh, B.K., et al., *Preparation of Cu nanoparticle loaded SBA-15 and their excellent catalytic activity in reduction of variety of dyes.* Powder Technology, 2015. **269**: p. 371-378.
87. Mokhtar, A., et al., *Improved stability of starch@ layered-materials composite films for methylene blue dye adsorption in aqueous solution.* Journal of Inorganic and Organometallic Polymers and Materials, 2020. **30**(9): p. 3826-3831.
88. Mekki, A., et al., *Fe and Ni nanoparticles-loaded zeolites as effective catalysts for catalytic reduction of organic pollutants.* Microporous and Mesoporous Materials, 2021. **310**: p. 110597.
89. Khan, S.A., et al., *Chitosan coated NiAl layered double hydroxide microsphere templated zero-valent metal NPs for environmental remediation.* Journal of Cleaner Production, 2021. **285**: p. 124830.

90. Khan, S.A., et al., *Reduction of nitrophenol isomers and degradation of azo dyes through zero-valent Ni nanoparticles anchored on cellulose acetate coated Ce/Zr composite.* Journal of Water Process Engineering, 2021. **44**: p. 102383.
91. Yao, T., et al., *A simple way to prepare Au@ polypyrrole/Fe 3 O 4 hollow capsules with high stability and their application in catalytic reduction of methylene blue dye.* Nanoscale, 2014. **6**(13): p. 7666-7674.
92. Xie, Y., et al., *Highly regenerable mussel-inspired Fe3O4@ polydopamine-Ag core–shell microspheres as catalyst and adsorbent for methylene blue removal.* ACS applied materials & interfaces, 2014. **6**(11): p. 8845-8852.
93. Khan, M.M., J. Lee, and M.H. Cho, *Au@ TiO2 nanocomposites for the catalytic degradation of methyl orange and methylene blue: an electron relay effect.* Journal of Industrial and Engineering Chemistry, 2014. **20**(4): p. 1584-1590.
94. Luo, J., et al., *Tannic acid functionalized graphene hydrogel for entrapping gold nanoparticles with high catalytic performance toward dye reduction.* Journal of hazardous materials, 2015. **300**: p. 615-623.
95. Liao, G., et al., *In-situ construction of novel silver nanoparticle decorated polymeric spheres as highly active and stable catalysts for reduction of methylene blue dye.* Applied Catalysis A: General, 2018. **549**: p. 102-111.
96. Khedkar, C.V., et al., *Magnetically separable Ag-Fe3O4 catalyst for the reduction of organic dyes.* Chemical Physics Letters, 2020. **742**: p. 137131.
97. Hachemaoui, M., et al., *M (M: Cu, Co, Cr or Fe) nanoparticles-loaded metal-organic framework MIL-101 (Cr) material by sonication process: catalytic activity and antibacterial properties.* Microporous and Mesoporous Materials, 2021. **323**: p. 111244.

Highlights

- $NiFe_2O_4$ catalysts were successfully synthesized by varying counter anions via facile coprecipitation method.

- Compatibility between chloride and nitrate counter-ion resulting in best catalytic reduction activity and NPs-size.

- The best nanocatalyst exhibited important saturation magnetization about 67.79 emu/g.

- The designed nanocatalyst can be reused five cycles without the influence of its efficiency.

Declaration of interests

☒ The authors declare that they have no known competing financial interests or personal relationships that could have appeared to influence the work reported in this paper.

☐The authors declare the following financial interests/personal relationships which may be considered as potential competing interests: